

A new computerized ionosphere tomography model using the mapping function and an application to the study of seismic-ionosphere disturbance

Jian Kong¹ · Yibin Yao² · Lei Liu² · Changzhi Zhai² · Zemin Wang¹

Received: 23 October 2015 / Accepted: 13 April 2016 / Published online: 4 May 2016
© Springer-Verlag Berlin Heidelberg 2016

Abstract A new algorithm for ionosphere tomography using the mapping function is proposed in this paper. First, the new solution splits the integration process into four layers along the observation ray, and then, the single-layer model (SLM) is applied to each integration part using a mapping function. Next, the model parameters are estimated layer by layer with the Kalman filtering method by introducing the scale factor (SF) γ to solve the ill-posed problem. Finally, the inversed images of different layers are combined into the final CIT image. We utilized simulated data from 23 IGS GPS stations around Europe to verify the estimation accuracy of the new algorithm; the results show that the new CIT model has better accuracy than the SLM in dense data areas and the CIT residuals are more closely grouped. The stability of the new algorithm is discussed by analyzing model accuracy under different error levels (the max errors are 5TECU, 10TECU, 15TECU, respectively). In addition, the key preset parameter, $SF\gamma$, which is given by the International Reference Ionosphere model (IRI2012). The experiment is designed to test the sensitivity of the new algorithm to SF variations. The results show that the IRI2012 is capable of providing initial SF values. Also in this paper, the seismic-ionosphere disturbance (SID) of the 2011 Japan earthquake is studied using the new CIT algorithm. Combined with the TEC time sequence of Sat.15, we find that the SID occurrence time and reaction area are highly related to the main shock time and epicenter. According to CIT images, there is a clear vertical electron density upward movement (from the 150-km layer to the

450-km layer) during this SID event; however, the peak value areas in the different layers were different, which means that the horizontal movement velocity is not consistent among the layers. The potential physical triggering mechanism is also discussed in this paper. Compared with the SLM, the RMS of the new CIT model is improved by 16.78%, while the CIT model could provide the three-dimensional variation in the ionosphere.

Keywords Mapping function · Computerized ionosphere tomography · Kalman filtering · Seismic-ionosphere disturbance · TEC variation sequence · Electric field effect

1 Introduction

Multi-dimensional ionosphere monitoring greatly improves the study of the ionosphere, as the multi-dimensional ionosphere models can reflect the horizontal variation of multiple layers and effect of electron coupling in the vertical direction. This is helpful in improving our understanding of ionosphere properties and in providing more extensive information for study of disaster ionospheric disturbances (Hajj et al. 1994; Hernandez-Pajares et al. 1999). Hajj et al. introduced computerized ionosphere tomography (CIT) in 1994. But until to 1997, the CIT algorithm realized by Rius with the Kalman filtering for the first time when GPS/MET occultation data from 28 stations and 160 IGS stations are combined to successfully invert three-dimensional ionosphere images (Rius et al. 1997).

Due to poorly sampled observations at the edge of the inversion region and the near-vertical signals observed from GNSS satellites containing little horizontal information, CIT is a typical ill-posed problem; in the presence of measurement errors, the estimated solution is extremely unstable.

✉ Yibin Yao
ybyao@whu.edu.cn

¹ Chinese Antarctic Center of Surveying and Mapping, Wuhan University, Wuhan 430079, China

² School of Geodesy and Geomatics, Wuhan University, Wuhan 430079, China

Ionosphere researchers continue to investigate the CIT algorithm in an effort to improve accuracy and stability. Thus far, CIT algorithms can be divided into two categories: function-based models (FBMs) and pixel-based models (PBMs). FBMs represent electron density of different layers with a group of basic functions, while PBMs represent electron density in discretized grids (pixels). These two types of models have been developed in parallel, and each has both pros and cons.

In 1992, Fremouw proposed that vertical ionosphere variation could be expressed by the empirical orthogonal function. Hansen (1998) explicitly states FBM estimation formulas and obtains the ionospheric electron density distribution using wide area augmentation system (WAAS) observation data. Howe et al. (1998) extended the inverted area to the entire scope of the ionosphere, resulting in three-dimensional time-varying ionosphere images produced with simulated GPS data and Kalman filtering. Gao and Liu (2002) proposed a real-time FBM that integrates the TEC smoothing model with the FBM; their model improves computation efficiency. Brunini et al. (2004) proposed a FBM based on the spherical harmonic and Chapman functions. Schmidt et al. (2008) and Limberger et al. (2013) investigated the stability and feasibility of an ionosphere tomography model based on the B-spline function. Alizadeh et al. (2015) developed a global three-dimensional ionosphere model based on the Chapman function by applying the ray tracing technique to the upper atmosphere.

The algorithm reconstruction technique (ART), multiplicative algorithm reconstruction technique (MART) and simultaneous iteration reconstruction technique (SIRT) (Avinash and Malcolm 1988; Pryse and Kersley 1992) are currently the more mature and commonly used PBM reconstruction algorithms. Modifications have been subsequently proposed to improve these three algorithms. Stolle et al. (2003) introduced constraints to the ART to ensure the stability of the solution. Yavuz et al. (2005) inverted three-dimensional ionosphere images and combined the total least sequence (TLS) with the ART, and then introduced the error-in-variable (EIV) model for ionosphere tomography. Nesterov and Kunitsyn (2011) applied a regularization constraint to the SIRT to solve the ill-posed problem. To improve CIT accuracy Wen et al. (2012) proposed a two-step method for inverting CIT images. First, the initial grid (pixel) values of electron density are estimated by the Phillips Smooth method; then, the MART is used to modify the initial value. To obtain varying real-time information based on the PBM, Yao et al. (2015) proposed a PBM algorithm with two-grid constraints and velocity parameters. However, the ill-posed problems are still the critical issues for the CIT algorithms affecting accuracy and stability of the CIT.

Ionosphere anomaly detection, especially of related ionosphere anomalies and ionosphere scintillation before

natural disasters (e.g., tsunamis, earthquakes, thunderstorms) is a currently a popular research topic (Pulinets and Boyarchuk 2004, Chapter 1.2, 1.5). Geophysical and geochemical anomalies occur directly preceding or during earthquakes; these anomalies include a rise in geothermal energy near the epicenter, the emission of chemical gases (e.g., Rn, CO₂), abrupt changes in tropospheric water vapor, and electron content anomalies in the ionosphere (Cervone et al. 2006; Oyama et al. 2008). Among these disturbances, the pre-earthquake ionosphere anomaly (PEIA) and co-seismic ionospheric disturbances (CID or SID in some papers) are the two short-period delayed cursors. Ionospheric anomalies associated with earthquakes were first presented in 1965 when Davies and Baker (1965) and Leonard and Barnes (1965) investigated ionosphere disturbances over the epicenter of the 1964 Alaskan Mag = 9.0 earthquake and found that the electron density showed a distinct disturbance in the hours before the earthquake. Initially, SID studies were limited to the confirmation of ionospheric anomalies in a single earthquake and associated statistical tests. However, more recently the statistical properties of SID occurrence (i.e., location and time) have been investigated (Dautermann et al. 2007; Liu et al. 2006; Kon et al. 2011; Saroso et al. 2008; Yao et al. 2012). With the increasing availability of ionosphere information, CIT, and other proposed detection methods, the features of SID can be investigated more comprehensively (Liu et al. 2010; Hao et al. 2013; Jin et al. 2014). Jin et al. (2015) proposed the concept of ionospheric seismology and theoretically summarized the current research achievements of physical SID mechanisms. With the CIT method, the three-dimensional reconstruction of electron density under SID is useful in tracking and understanding the evolution of this process; this then allows for further study of physical mechanisms.

2 MFCIT estimation model

2.1 The principle

Currently, the SLM is the main tool for studying ionosphere variation due to its simplicity and capability for monitoring the state of the global ionosphere. SLMs are used to obtain the total electron content (TEC) in near-real time and are used in ionosphere delay corrections of navigation as well as monitoring of the space environment. The global ionosphere maps (GIM) from International GNSS Service (IGS) is also based on SLM. However, SLM cannot present vertical ionosphere variations and are imperfect compared with the CIT model theoretically due to errors from the model hypothesis. Especially in monitoring of the space environment, SLM cannot present the coupling interaction amongst layers at different altitudes. CIT algorithms, which are divided to two types—FBMs and PBMs—are subject to typical ill-posed problems;

therefore, even the CIT model is theoretically better than SLM, the CIT solution is very unstable.

Here, we propose a new FBM tomography algorithm, MFCIT (CIT using mapping function), which considers the basic variations of ionosphere characteristics. MFCIT decreases the number of tomography layers required to make solution stable. In each layer, the SLM and the mapping function are simultaneously applied to improve model accuracy. Multi-dimensional ionosphere variation information can also be presented with the multi-layer images.

When the GNSS signals pass through the ionosphere, delay effects, which is proportional to the electron density along the line of sight (LOS), should be considered. The electron density can be expressed by the TEC [slant TEC (STEC)] is the integration of the electron density along the LOS). STEC can be transferred to vertical TEC (VTEC) using the mapping function (Formula 2).

$$STEC(t) = \int_s Ne(s, t) ds \tag{1}$$

$$VTEC(t) = STEC(t)/MapFunc = STEC(t)/MF, \tag{2}$$

where s is the LOS, t is the observation time, $Ne(s, t)$ is the electron density function along the LOS, and MapFunc is the mapping function.

To show multi-ionosphere morphology, Formula (1) is split into several parts with each part representing a layer in ionosphere (Fig. 1, Formula 3). The number of splits to make the solution stable is between 3 and 5 according to our experiments. As when the layer numbers are over 5, the model parameters in formula (4) among different layers are strongly related, thereby making the solution unstable.

$$\begin{aligned} STEC(t) &= \int_s Ne(s, t) ds \\ &= \int_{h=0}^{h=300} Ne(s, t) ds + \int_{h=300}^{h=600} Ne(s, t) ds \\ &\quad + \int_{h=600}^{h=900} Ne(s, t) ds + \int_{h=900}^{h=1200} Ne(s, t) ds \\ &= VTEC_{150} \times MF_{150} \times VTEC_{450} \times MF_{450} + VTEC_{750} \\ &\quad \times MF_{750} + VTEC_{1050} \times MF_{1050} \end{aligned} \tag{3}$$

During each integration intermediate heights are used to represent the electron density of each layer (i.e., 150-km layer height represents the electron density ranging from 0 to 300 km) and the SLM is applied by transferring the STEC to VTEC with MF (Formula 3). Here the integration range is divided to four equal parts (the first part includes D-layer and E-layer, while the second part include F-layer), and the division method according to the ionosphere physical properties (D-layer 50–90 km, E-layer 90–130 km, F1-layer 130–210 km, F2-layer >210 km) is not suggested. As this method will make the solution unstable, this issue will be discussed in Sect. 2.3.

$$\begin{aligned} VTEC_{150} &= \sum_{i=0}^n \sum_{j=0}^m A_{ij} (b - b_0)^i (s - s_0)^j \\ &= a_{00} + a_{01}b + a_{02}s + a_{03}bs + a_{04}b^2 \end{aligned} \tag{4.1}$$

$$s - s_0 = (l - l_0) + (t - t_0) \tag{4.2}$$

$$MF = \frac{1}{\cos(z')} = \frac{1}{\sqrt{1 - \sin^2(z')}} \tag{5}$$

In Formula (4), the second-order polynomial model is chosen as an example, n, m are the orders in latitude

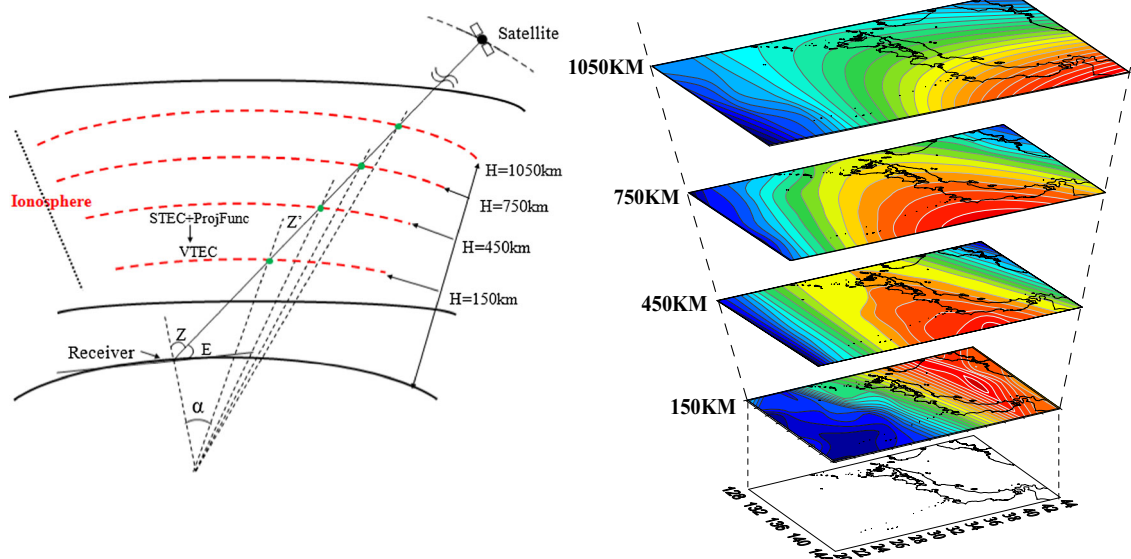


Fig. 1 Schematic diagram of the new CIT model

and longitude, respectively. Formula (5) gives the modified SLM mapping function from CODE, where; $\sin(z') = \frac{R}{R+H} \sin(\alpha z)$, $R = 6371$ km, H is the assumed ionosphere height, $\alpha = 0.9782/z$ is the zenith angle at the ionosphere piece point (IPP), s_0 is the solar hour angle at center point (b_0, l_0) of the interested area and the middle time of the interested time span, b_0, l_0 is the latitude and longitude at center point, and b, l are the latitude and longitude of the IPP. Substituting Formulas (4) and (5) into Formula (3), the estimated function model of MFCIT is derived (Formula 6, ignoring the observation time symbol).

$$\begin{aligned} \text{STEC} = & (a_{11} + a_{12}b_{150} + a_{13}s_{150} + a_{14}b_{150}s_{150} \\ & + a_{15}b_{150}^2) \times \text{MF}_{150} \\ & + (a_{21} + a_{22}b_{450} + a_{23}s_{450} + a_{24}b_{450}s_{450} \\ & + a_{25}b_{450}^2) \times \text{MF}_{450} \\ & + (a_{31} + a_{32}b_{750} + a_{33}s_{750} + a_{34}b_{750}s_{750} \\ & + a_{35}b_{750}^2) \times \text{MF}_{750} \\ & + (a_{41} + a_{42}b_{1050} + a_{43}s_{1050} + a_{44}b_{1050}s_{1050} \\ & + a_{45}b_{1050}^2) \times \text{MF}_{1050} \end{aligned} \quad (6)$$

where a_{11} – a_{45} are the estimated parameters, STEC is the observation, b_i, s_i ($i = 150, \dots, 1050$) are the latitude and longitude of IPPs on each layer and MF_i ($i = 150, \dots, 1050$) are the mapping functions of each layers (Fig. 1).

2.2 SLM and mapping function

In SLM the ionospheric electron density is assumed to be concentrated on a thin layer (usually chosen at 450 km) and the mapping function should be applied to transfer STEC to VTEC. There are two main problems with this approach: first, the global peak height of the ionosphere is not consistent on a global scale, and differences of hundreds of

kilometers may exist at the same time (Hernández-Pajares et al. 2005); second, the mapping function may introduce significant (greater than 5 %) error (Hernández-Pajares et al. 2010). All CIT models could easily eliminate the errors due to variations in global peak height with electron densities estimated in three-dimensions. The mapping function is still used in MFCIT, but as shown below, we argue that model errors from the mapping function are greatly reduced. In this paper, the elevation mask angles of the experiments are set at 25°.

The transformation from STEC to VTEC can also be taken as a linear integration process (Formula 7, Fig. 2).

$$\frac{d\text{VTEC}}{d\text{STEC}} = \cos(Z') \rightarrow d\text{VTEC} = \cos(Z')d\text{STEC} \quad (7)$$

where $d\text{VTEC}$ is the TEC differential variable in the vertical direction, $d\text{STEC}$ is the TEC differential variable along the LOS, and Z' is the zenith angle at the point ds (Fig. 2). By integrating both sides:

$$\begin{aligned} \int (d\text{VTEC})ds &= \int \cos(Z')d\text{STEC}ds \\ &= \cos(Z') \int (d\text{STEC})ds \end{aligned} \quad (8)$$

$\int (d\text{STEC})ds$ (observation STEC) is easy to compute. The variation of Z' is not considered within a small area, so $\cos(Z')$ is a constant and free from ds . The difficult integration is $\int (d\text{VTEC})ds$, as the fundamental equation between VTEC and ds is unknown. In theory, the integration cannot be completed; however, in the SLM (Fig. 2b), VTEC is expressed by the latitude and longitude at a certain altitude (Formula 9).

$$\text{VTEC} = f(b, l) \quad (9)$$

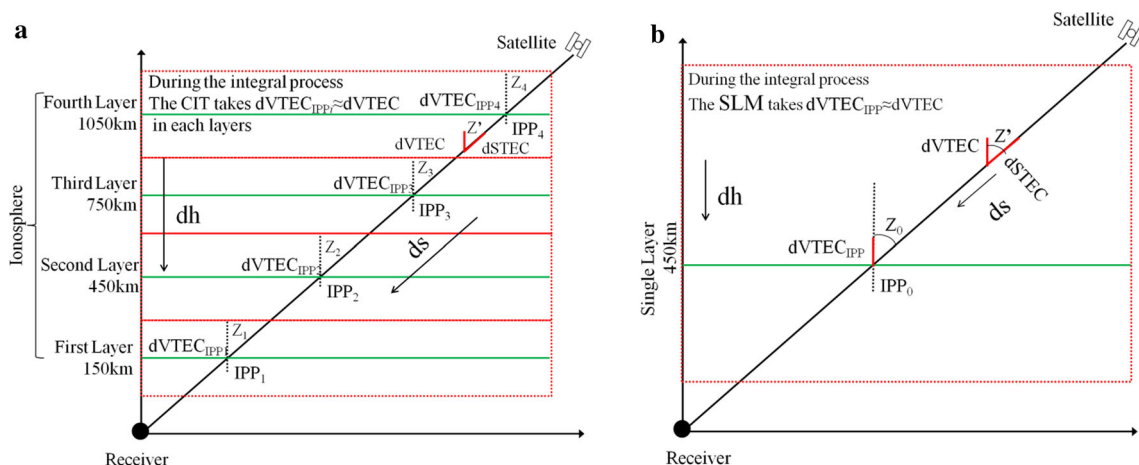


Fig. 2 Model errors from mapping functions of the CIT model (a) and SLM (b)

In the SLM the electron density is concentrated on a single layer, so $ds = dh$ and the integration along the LOS is transferred to the vertical direction (Fig. 2b). Further, dh is replaced by $dh_{(b_0, l_0)}$ at the IPP:

$$\begin{aligned} \text{VTEC}_{\text{SLM}} &: \int (d\text{VTEC})ds \approx \int (d\text{VTEC})dh \\ &= \int (d\text{VTEC})dh_{(b,l)} = f(b, l) \\ \cos(Z') &= \frac{f(b, l)}{\text{STEC}} = \frac{\text{VTEC}_{\text{SLM}}}{\text{STEC}} \end{aligned} \tag{10}$$

where (b, l) are the latitude and longitude at the IPP. $d\text{VTEC}_{\text{IPP}}$ at dh ($d\text{VTEC}_{\text{IPP}}$, Fig. 2b) is not consistent with that at ds ($d\text{VTEC}$, Fig. 2b); the difference between the two $d\text{VTECs}$ may become large when the elevation angle is low (Formula 10, Fig. 2b) (Hernández-Pajares et al. 2010). This is one of the main errors in the SLM.

In MFCIT one observation ray has IPPs for each layer, and the number of IPPs is the layer number (Fig. 2a). Therefore, when integrating ds is replaced by dh , and the $d\text{VTECs}$ are closer (Formula 11).

$$\begin{aligned} \text{VTEC}_{150} &: \int (d\text{VTEC})ds_1 \approx \int (d\text{VTEC}_{\text{IPP1}})dh_1 = f_{150}(b_{150}, l_{150}), \dots \\ \text{VTEC}_{1050} &: \int (d\text{VTEC})ds_4 \approx \int (d\text{VTEC}_{\text{IPP4}})dh_4 = f_{1050}(b_{1050}, l_{1050}) \\ \cos(Z') &= \frac{f_{150}(b_{150}, l_{150}) + f_{450}(b_{450}, l_{450}) + f_{750}(b_{750}, l_{750}) + f_{1050}(b_{1050}, l_{1050})}{\text{STEC}} \\ &= \frac{\text{VTEC}_{150} + \text{VTEC}_{450} + \text{VTEC}_{750} + \text{VTEC}_{1050}}{\text{STEC}} \end{aligned} \tag{11}$$

vertical ionosphere structure. The planimetric positions of IPPs on each layer are very close (Fig. 2a, IPP₁–IPP₄). So, the solution is unstable because the condition numbers of normal equations are very large. This is the reason why integration range is not suggested to be divided according to the ionosphere physical properties, in that case the IPP_{*i*} are very difficult to distinguish. Estimation models (Formula 6) also need to solve this problem.

There are many ways to address this issue (Bhuyan et al. 2002). In this paper, the iterative solution with Kalman filter is used. After the integration is split into 3–5 parts, the model parameters of each integration (i.e., layer) are computed step by step by introducing $SF\gamma_i$. The model parameters of the 150-km layer are solved first by $SF_{150\text{ km}} = 0.3$ (Formula 12.1).

$$\begin{aligned} \text{STEC} &\quad \gamma_{150} (0 < \gamma_{150} < 1) \\ \text{First step} & \\ \text{Observation equation} & \\ \begin{cases} \gamma_{150} \times \text{STEC} = (a_{11} + a_{12}b + a_{13}l + a_{14}bl + a_{15}b^2) \times \text{MF}_{150} \\ A_1 = (a_{11} \ a_{12} \ a_{13} \ a_{14} \ a_{15}) \end{cases} & \\ \Rightarrow A_{1\text{EST}} \quad Q_{A_{1\text{EST}}} & \end{aligned} \tag{12.1}$$

2.3 Iterative solution

CIT is a typical ill-posed problem mainly because navigation satellites' (i.e., GPS, GALILEO, GLONASS and COMPASS) orbits are at a height over 20,000 km and the observed signals from the satellites contain little information of the

After first step, the estimated parameters ($A_{1\text{EST}}$) and accuracy information ($Q_{A_{1\text{EST}}}$) of the 150-km layer are considered in next estimation step as the initial value (L_{A_1} , Formula 12.2), while $Q_{L_{A_1}}$ is used to add the accuracy constraint. With $SF_{150\text{ km}} = 0.3$ and $SF_{450\text{ km}} = 0.5$:

Fig. 3 Distributions of stations (a) and IPPs (b)

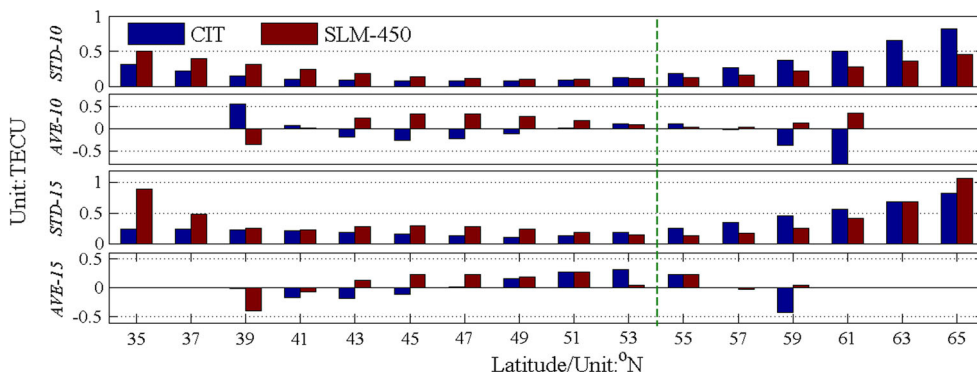
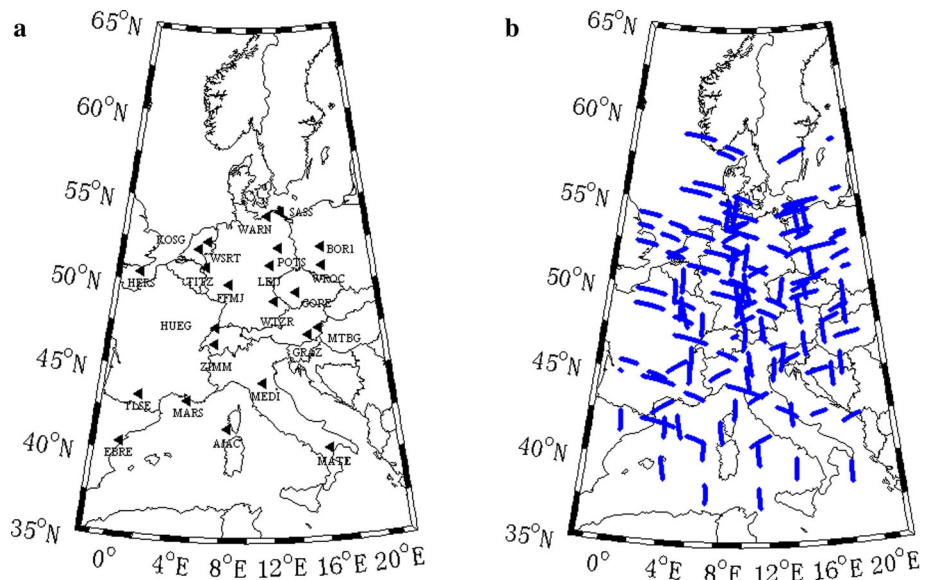


Fig. 4 Comparison of statistical accuracy between the CIT and SLM on different latitude surfaces

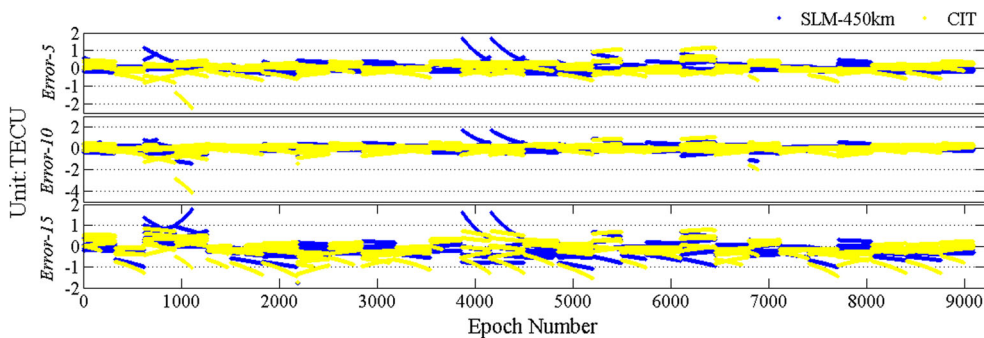


Fig. 5 Comparison of residual sequences between the CIT and SLM under different error groups

and $STEC_{SLM-450\text{ km}}$ (i.e., SLM STEC sequence, with layer height at 450 km, SLM-450 km).

The CIT model accuracy is improved slightly compared with the SLM (Fig. 4). Specifically, there is improvement between 35°N and 53°N, while accuracy decreases between 55°N and 65°N compared with the SLM. This is mainly because of the distribution of observations, as the IPPs are

mostly distributed between 40°N and 55°N (Fig. 3b). The SLM model is simpler (less parameters), so the estimation of TEC in the SLM is more stable than in the CIT model (more complex model) in the area with sparse or no observations. Figure 5 demonstrates the residual sequence of two models under different error group. From the figure, the CIT residuals are grouped in smaller regions.

3.1.2 Robustness of the MFCIT model

To test the validity and robustness of the proposed iterative solution (Sect. 2.3), the value $VTEC_{CIT}$ was subtracted from the estimated values $VTEC_{CIT}$ (CIT VTEC) for different layers under different levels of errors (Max = 5, 10, 15). Figure 6 presents the error distribution of different layers and the accumulated error of four layers. For convenience, in the figure, the legend is ranging from -0.5 to 1 for the layers

at height 150, 450 km and the accumulated layer, while it is from -0.5 to 0.5 for the other layers.

As the error (MAX) increases, CIT accuracy is not decreased badly (Fig. 6). Under the error group Max = 5TECU, the total residuals are randomly distributed among those of layer 450 km. Between 40°N and 50°N , the total residuals are almost 1 TECU; for layer 450 km, the residuals are nearly 0 in the same area. Therefore, total residuals are a result of the left three layers. With increasing error lev-

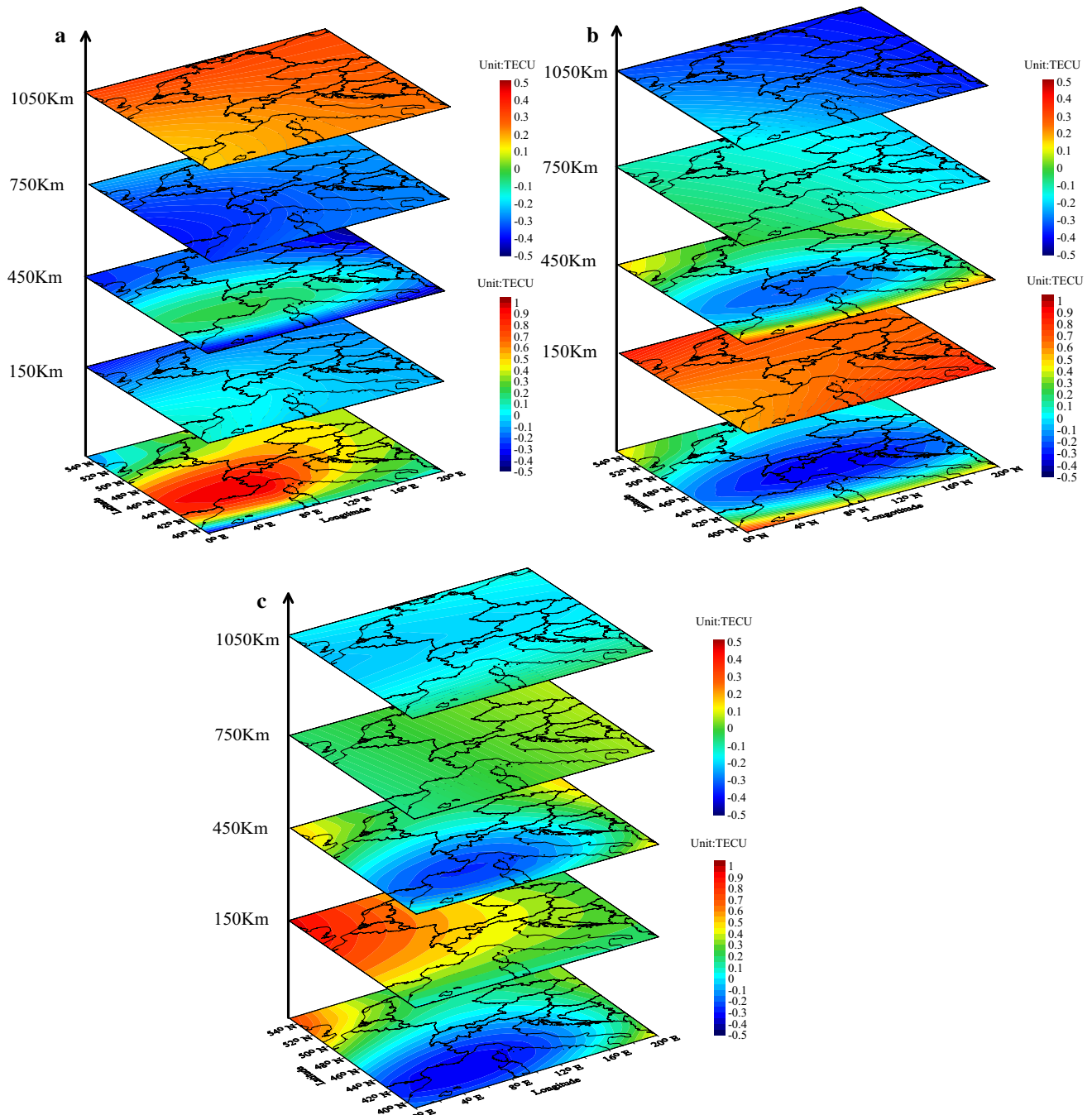


Fig. 6 True error distribution of CIT model under error groups Max = 5TECU (a), Max = 10TECU (b), Max = 15TECU (c)

els (Max = 10TECU, 15TECU) the distribution of the total residuals and residuals on 450-km layer are consistent. This means that CIT accuracy is mainly influenced by parameter estimation on the 450-km layer; this should be taken into consideration when process noise from this layer is input into the iterative solution.

3.1.3 Impact of SF initial values

SF is an artificial parameter and is key factor for adjustment (Formula 12). In this paper, SF is suggested to be determined by the IRI2012 model (Bilitza et al. 2011) because the SF from IRI satisfies the accuracy requirement according to our test. In this section, experiments are designed to test the sensitivity of MFCIT to SF variation.

First, we compared the initial SF values with those after adjustment. Before adjustment $SF\gamma$ is artificially set; after adjustment SF γ_{Est} is automatically changed based on real ionosphere conditions (Formula 15):

$$\gamma_i^{Est} = \frac{VTEC_i}{VTEC_{150} + VTEC_{450} + VTEC_{750} + VTEC_{1050}} \quad (i = 150, 450, 750, 1050) \quad (15)$$

Figure 7 gives the γ_i^{Est} distribution on layer 150 km and layer 450 km with the error group Max = 10. Before adjustment, $\gamma_{150} = 0.2$, $\gamma_{450} = 0.6$, respectively.

In the 150-km layer, γ_{150}^{Est} ranges from 0.1 to 0.3; in the 450-km layer γ_{450}^{Est} ranges from 0.5 to 0.8. Although SFs are artificially set before adjustment and there is only one constant value in each layer, after the adjustment the SFs are regulated automatically to optimally satisfy the estimation process. For example, on the left top part of Fig. 7, γ_{150}^{Est} increases to ~ 0.23 while γ_{450}^{Est} decreases to ~ 0.55 (Fig. 7).

To further analyze the impact of SF variation on estimation stability, different groups of SFs were introduced to the estimation process under the Max = 10 TECU error group

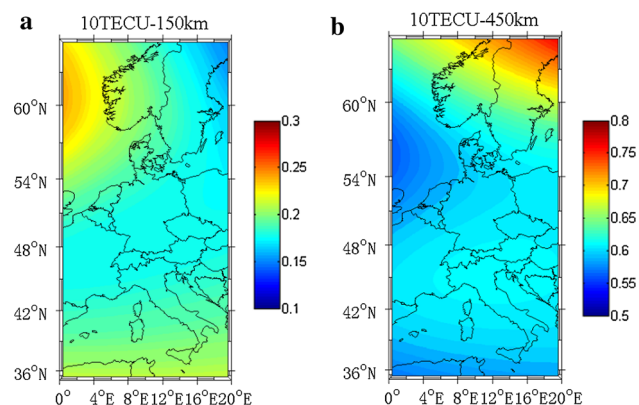


Fig. 7 SF values for the 150 km (a) and 450 km (b) layers with the error group Max = 10TECU

Table 1 Different groups of SFs

	150 km	450 km	750 km	1050 km
1	0.20	0.60	0.15	0.05
2	0.25	0.55	0.10	0.10
3	0.30	0.50	0.05	0.15
4	0.40	0.40	0.05	0.15

(Table 1). The first group of SFs contains no error; then, from group 2–4, the SF accuracy worsens (Table 1). This suggests that the errors in SFs on the 150 and 450-km layers continue to increase and the electron density of the two layers accounts for most ($\sim 80\%$) of the total electron density.

Take the $VTEC_{CIT}$ of group 1 SFs as background, the comparison between group 1 estimation and each groups' estimation are shown in Fig. 8 (from top to bottom the figure presents the error distribution of different layers and the accumulated error of four layers). With the accuracy of the γ sets decreasing, the estimation difference from group 2 to group 4 increases. The difference between group 2 and group 1 is within 1.5TECU (Fig. 8a). Even though the SFs deviate by 10% from the real values, the estimated differences are less than 2TECU (Fig. 8b). However, the differences on different layers are complementary so the resulting total difference of the four layers is near zero (within 0.5TECU). In Fig. 8c, the largest difference is almost 5TECU on the 450-km layer, and the total differences of all layers are (-2 to -3) TECU, with the SFs offsetting by 20% for the 150 and 450-km layers in group 4.

Based on experimental results the electron density difference could be less than 2TECU if the errors of SF initial values are within 10%. The major data sources of IRI are the worldwide network of ionosondes (i.e., powerful incoherent scatter radars) using the newest version of IRI2012. As IRI could calculate the electron density on different layers, the VTEC on each integration part (i.e. from 300 to 600 km) could be obtained by integrated the IRI electron density. The initial SF values from IRI2012 fully meet the accuracy requirements (Bilitza et al. 2012).

3.2 A SID case study

Real measurement data of the IGS tracking network was used to reconstruct three-dimensional ionosphere images around the co-seismic time of the 2011 Tohoku Earthquake. Figure 9 gives the Dst index, Kp index and the F10.7 Index sequence from March 1 to March 15. During the time, the F10.7 variations are greater than 100, and in particularly on March 8 the F10.7 peak is 155, exceeding 3% of its mean value. From March 1 to March 2 and March 10 to March 12 the Kp index is below 4 with a Dst index over $-40nT$; this shows

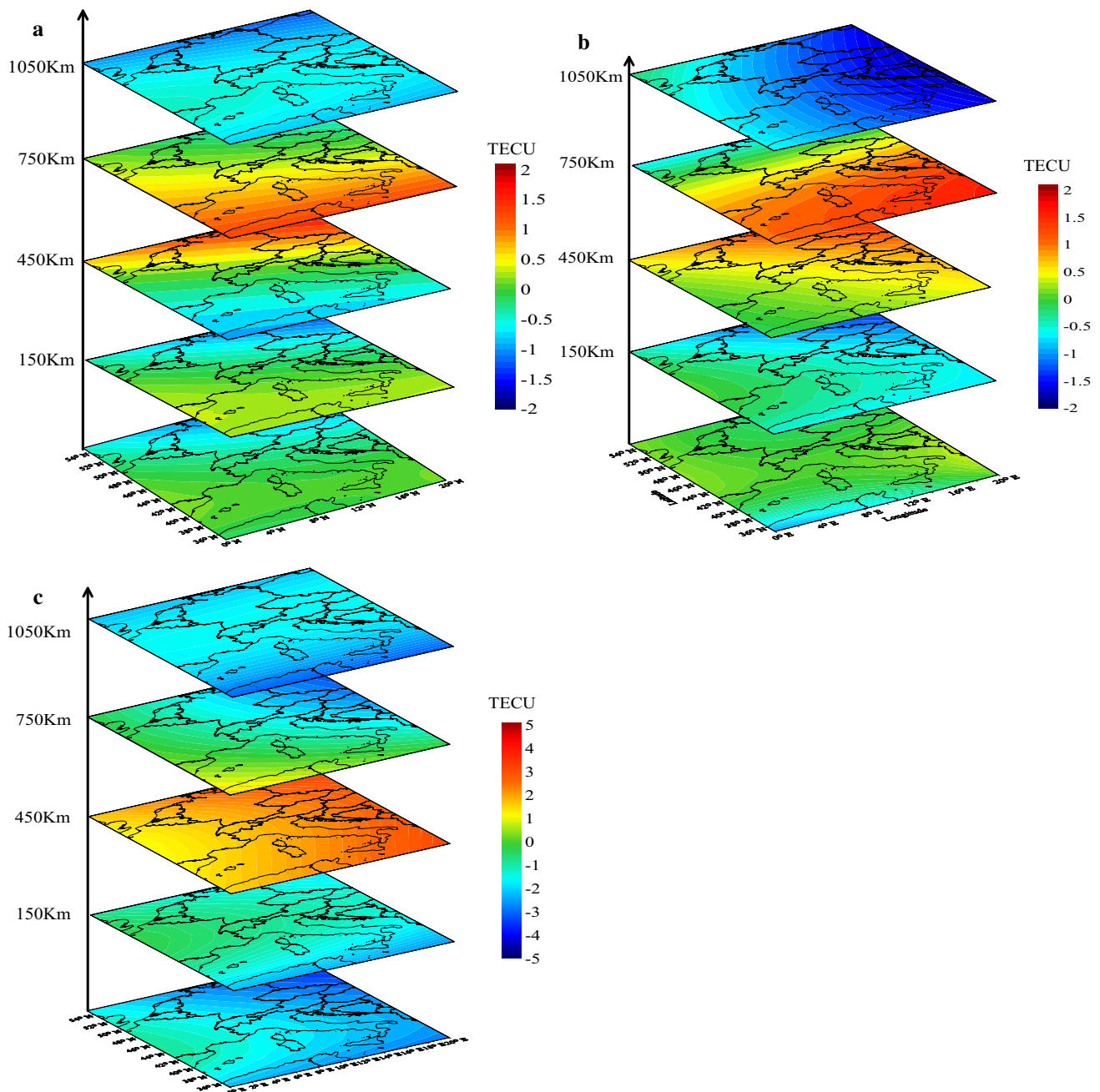


Fig. 8 Differences in ED (electron density) distribution value estimations between group 1 γ and group 2–4 under error Max = 10TECU: group 2 (a), group 3 (b), and group 4 (c)

slight geomagnetic disturbances on these four days. During the rest of the time the geomagnetic conditions are relative peaceful ($K_p < 4$, $Dst > -20\text{nT}$). In particular, on March 8 the K_p index variations were less than 2 and the Dst index variations were more than -20nT for the whole day, showing very calm geomagnetic conditions, so the images are chosen as the background in Fig. 12. On March 11, the main shock day, the K_p index is close to 6 at noon and the Dst index exceeds -50nT .

Figure 10 shows the IPPs location sequences of Satellite 15 observed on four IGS stations (MIZU, SMST, TSK2, and USUD). In order to illustrate the relationship of the IPPs location with the epicenter and occurring time of the TEC disturbance with the main shock time, in the figure, the occurring time of the TEC disturbance are marked with the red triangle, while the main shock time is marked with yellow triangle on the sequence (the occurring time of the TEC disturbance are defined in Fig. 11 with the red line). The pink line connects

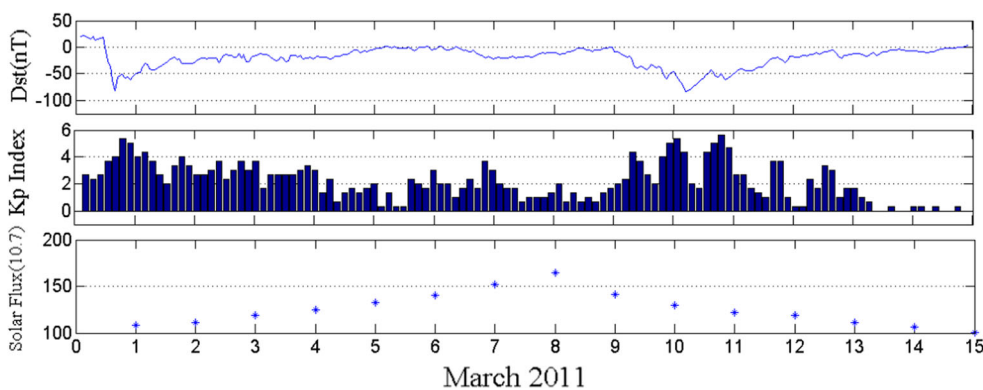


Fig. 9 Dst index, Kp index, and F10.7 index variation sequences from March 1 to March 15

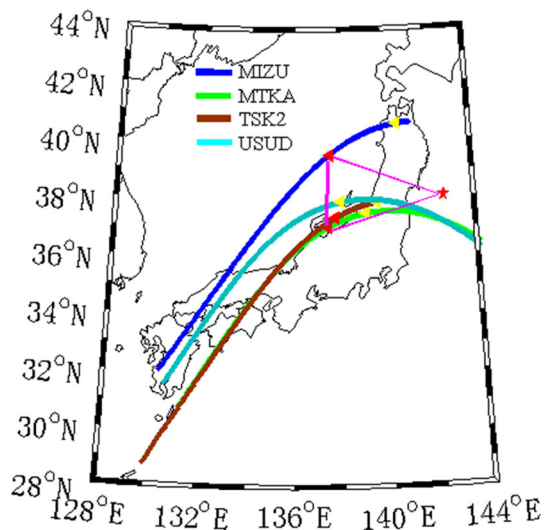


Fig. 10 IPP location sequences of Satellite 15 observed from four IGS stations. Red triangles correspond to the positions marked by the red line in Fig. 11. Yellow triangles correspond to the positions marked by the yellow line in Fig. 11. The red mark indicates the epicenter and the pink triangle indicates the SID reaction area. The pink line connects the epicenter and the outside two TEC disturbance points

the epicenter and the outside two TEC disturbance points, so the pink triangle is giving out the SID reacting area approximately.

In Fig. 11, the VTEC variation sequence of Satellite 15 observed on the above four stations shows that about one hour before the main shock time (marked with the yellow lines), the VTEC variation sequences experience the positive disturbance on the three stations (MIZU, TSK2, MTKA). As Heki and Enomoto (2013) proposed, due to different selection of ionosphere background values, this SID event can be explained by two opposing interpretations; positive or negative disturbance. In this paper, we prefer the positive one. The disturbances are within 5TECU. The reaction at MIZU is strongest, followed by TSK2, and then MTKA, even though the IPP sequence of MTKA is closest to the epicenter

(Fig. 10). The IPP trajectory of MTKA is parallel to the contours of the ED increase percentage, so the ED disturbance is less than the MIZU disturbance whose IPP trajectory cut across the contours (Figs. 10, 12).

The VTEC sequences of USUD fail to perform the positive disturbance and the sequences only show fluctuations. This can be attributed to the quality of observation data, as the fluctuations represent the instable accuracy of TEC from USUD.

Over the epicenter, SID shows typical waveform characteristics as reported by Maruyama et al. (2011) using ionosonde data. Additionally, the SID center is not right above the epicenter but shifted to the 144°E surface.

By comparing the SID images on different layers (i.e., 150 and 450 km) it is evident that the movement velocity of electron particles is not consistent. On March 8, the peak value area of the 150-km layer moves to the 128°E surface; meanwhile in the 450-km layer, the peak value area is still distributed on the 144°E surface. There are several factors impacting the horizontal movement of electrons, such as neutral wind, ion collisions, and magnetic force. At lower altitudes the collision frequency is greater than the gyro-magnetic frequency, and the ions move with neutral wind. However, at higher altitudes the gyro-magnetic frequency is much greater than the collision frequency and ions cannot cross magnetic field lines, unless, a neutral wind or an electric field set the plasma in a FxB motion; therefore, only the component of the velocity parallel to the magnetic lines is reserved. The movement velocity of electrons at different altitudes is theoretically inconsistent.

More importantly, during this SID event, there is strong vertical electron movement around the epicenter. Electron density experienced a substantial increase in the 450-km layer, while in the 150-km layer; the electron density experienced a sharp decrease (Fig. 12). This is likely caused by the vertical movement of electron density. Even so, considering the overall changes in all layers the electron density exhibits a positive disturbance.

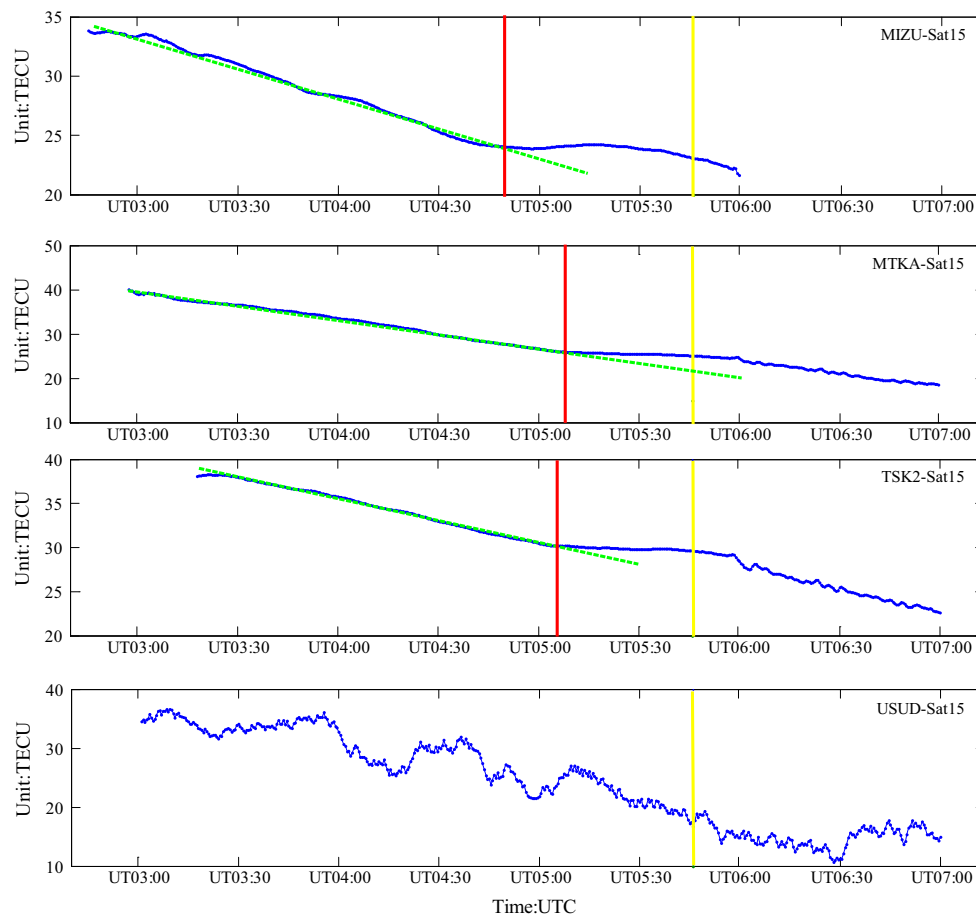


Fig. 11 VTEC variation sequences of Satellite 15 observed from four IGS Stations (the *green line* presents the VTEC sequence. The *red line* marks the TEC disturbance point and the *yellow line* marks the main shock time)

At present, the SID can be explained by two interpretations; the electric field effect and the propagation of atmospheric gravity waves. The electron vertical movement in this paper could result from electric field effect. Ionosphere dynamics associated with zonal (west-east) electric fields have been suggested by Pulnits et al. (2000) and Pulnits and Boyarchuk (2004, Chapter 4.3). During earthquakes, the accumulation of charge carriers over the Earth's surface produces positive surface charges (Boyarchuk et al. 1997). The perpendicular component of the electric field leads to plasma $E \times B$ motion (\times is cross product operation). The simulation results from the SAMI3 model show that the applied zonal electric field leads to TEC variations near the source region (i.e., a westward electric field causes a downward $E \times B$ motion of the ionosphere and an eastward electric field causes an upward $E \times B$ motion of the ionosphere). Due to the upward motion by an eastward electric field, the region of electron density increase at higher altitudes (i.e., 450 km) is larger than the region of electron density decrease at lower altitudes (i.e., 150 km). Therefore, an eastward electric field results in a decrease of TEC at lower

altitudes and an increase of TEC at higher altitudes (Kuo et al. 2014, Fig. 11). Theoretical research confirms our CIT results. In order to illustrate consistency between the 1D TEC disturbances of IPP sequences and the two-dimensional disturbances distribution of CIT images, in Fig. 12 we overlap the IPP trajectory in Fig. 11 on top of the Fig. 12. Even though there is a moderate geomagnetic storm on March 10, but different with ionosphere disturbance caused by storm (in global scale), the disturbances demonstrated in this paper are a regional reaction, while the reaction area and time are related with the epicenter and main shock time. So the ionosphere disturbance is possibly related with the seismic activity. Comparing with Fig. 10, the reacting areas are similar with the center area of ED (electron density) increase percent images.

The accuracy of the new CIT model is reconfirmed by statistical analysis of residuals of the SLM and MFCIT models (Table 2). The observations fit well under both of the two models as the interested areas at mid-latitudes and the electron density variations are relatively smooth. In SLM STD is 1.2709TECU, while the accuracy is improved by 16.78 %

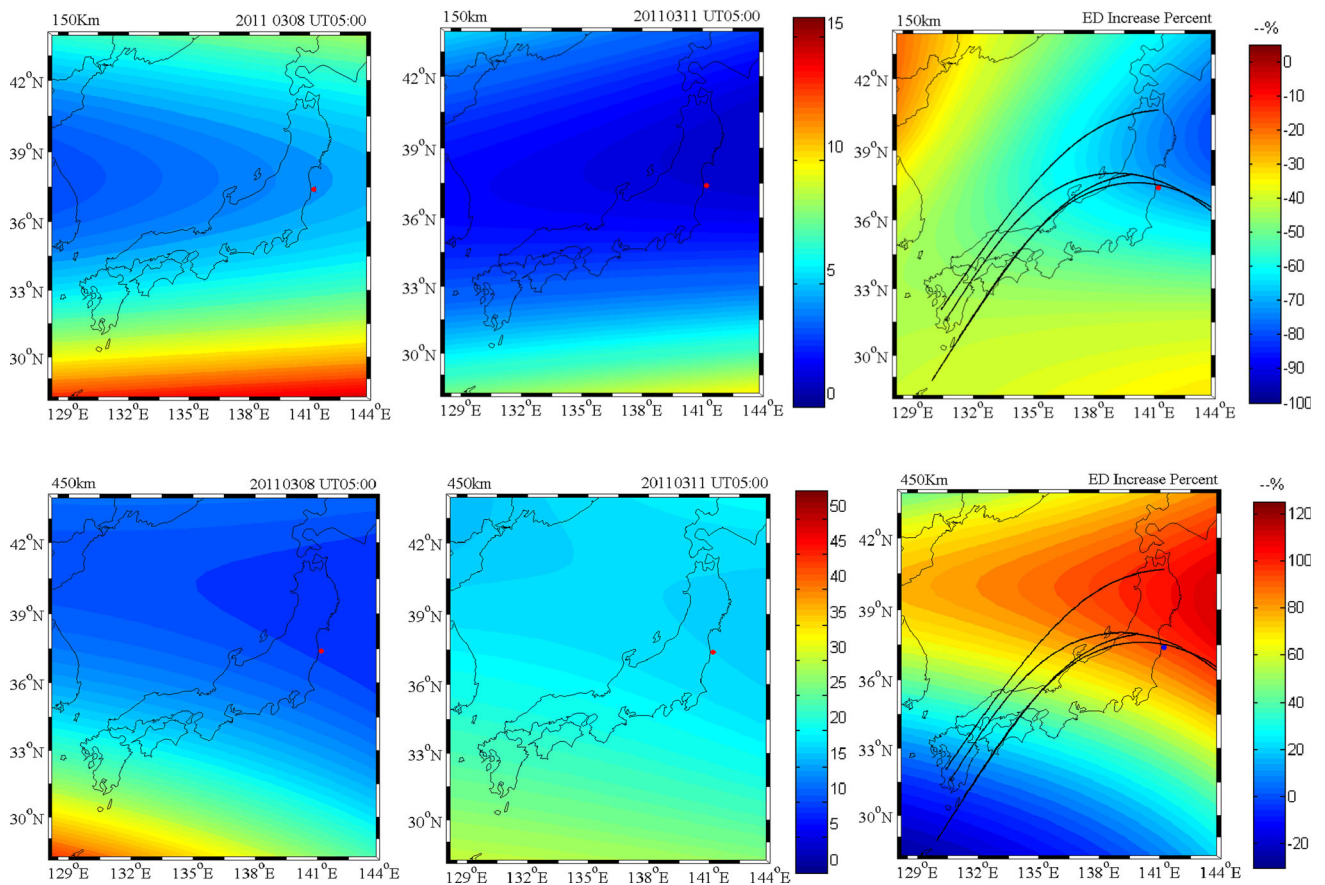


Fig. 12 ED distribution on 150 and 450-km layers on March 8 and March 11, and the ED increase in percent

Table 2 Statistical information of residuals under the SLM and new CIT models

	STD	AVER	MAX	MIN
SLM	1.2709	-0.1825	4.2951	-3.3966
MFCIT	1.0577	-0.1076	3.2591	-3.7105
%	16.78	41.02	24.12	-9.20

with the MFCIT model. When fitting the average value the accuracy is improved by 41.02 %.

The residuals sequence of the MFCIT model shows that 99 % of the residuals are within 3 TECU (Fig. 13). Thus, the MFCIT model proposed in this paper is reliable, and the accuracy is ensured for the monitoring of the space environment.

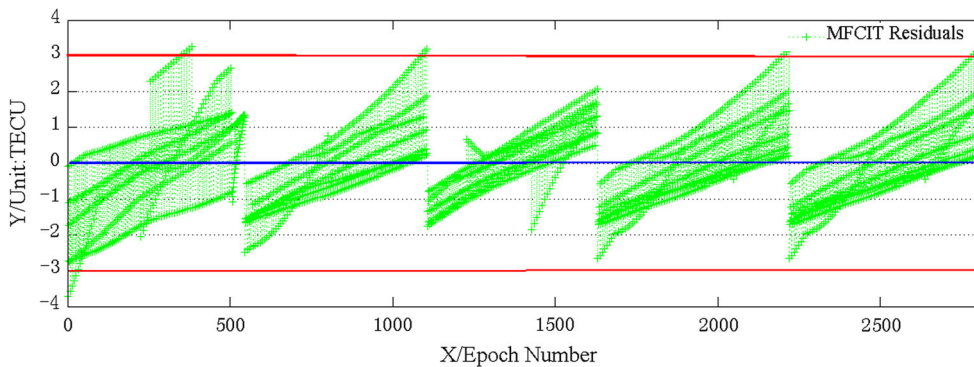


Fig. 13 Sequence of TEC residuals in the MFCIT model

4 Conclusion

In this paper, a new CIT model using a mapping function is proposed. Compared with traditional algorithms, the number of CIT layers is reduced as the ionospheric region has been separated by four artificial layers with corresponding mapping functions; as a result, model accuracy is ensured, while the images from different layers present spatial variation in the ionosphere. In order to solve the ill-posed problem, the iterative solution is used to ensure the estimation stability. By using the accuracy information from last step as the constraint and the introduction of SF factors, the parameters are estimated step by step with the Kalman filtering method. With the simulated data experiment, the feasibility and fitted accuracy of the new model is discussed and verified adequately. Additionally, the method for determining SF is given and the impact of error in the initial SF values on model accuracy is also analyzed.

A SID case study of the 2011 Japan Tohoku Earthquake was conducted with IGS data. First, the TEC sequences of Satellite 15 observed from four IGS stations are used to identify the SID reaction time and area. By connecting reaction points of the IPP sequences with the epicenter, the SID reaction area is determined to be consistent with the center area of increase in ED images from the CIT model. Based on the CIT images, there is a strong electron vertical movement among different layers of the ionosphere. There is a substantial increase in electron density for the 450-km layer, while in the 150-km layer the electron density sharply decreased. Finally, the potential physical triggering mechanism is also discussed, an eastward electric field maybe the dynamic source for this SID event.

Using real measurement data, 99 % of CIT residuals are within 3TECU. Compared with the SLM, the STD and AVER are improved by 16.78 and 41.02 %, respectively. The new CIT model has greater accuracy with more homogeneous observation distribution while simultaneously giving spatial features of the ionosphere.

In this paper, the same mapping function from CODE is used on different layers, but the effectiveness of the mapping function may decrease at higher lower altitude layers; the next step is to modify the mapping function.

References

- Alizadeh MM, Schuh H, Schmidt M (2015) Ray tracing technique for global 3-D modeling of ionospheric electron density using GNSS measurements. *Radio Sci* 50:539–553
- Avinash CK, Malcolm S (1988) Principles of computerized tomographic imaging, pp 275–296
- Bhuyan K, Singh SB, Bhuyuan PK (2002) Tomographic reconstruction of the ionosphere using generalized singular value decomposition. *Curr Sci* 83(9):1117–1120
- Bilitza D, McKinnell LA, Reinisch B, Fuller-Rowell T (2011) The international reference ionosphere (IRI) today and in the future. *J Geod* 85:909–920
- Bilitza D, Brown SA, Wang MY, Souza JR, Roddy PA (2012) Measurements and IRI model predictions during the recent solar minimum. *J Atmos Solar-Terr Phys* 86:99–106
- Boyarchuk KA, Lomonosov AM, Pulnits SA (1997) Electrode effect as an earthquake precursor. *BRAS Phys Suppl Phys Vib* 61(3):175–179
- Brunini C, Meza A, Azpilicueta F, Zele MAV, Gende M, Alejandro D (2004) A new ionosphere monitoring technology based on GPS. *Astrophysics and space science*, pp 415–429
- Cervone G, Maekawa S, Singh RP, Hayakawa M, Kafatos M, Shvets A (2006) Surface latent heat flux and nighttime LF anomalies prior to the Mw = 8.3 Tokachi-Oki earthquake. *Nat Hazards Earth Syst Sci* 6:109–114
- Dautermann T, Calais E, Haase J, Garrison J (2007) Investigation of ionospheric electron content variations before earthquakes in southern California, 2003–2004. *J Geophys Res* 112:B02106
- Davies K, Baker D (1965) Ionospheric effects observed around the time of the Alaskan earthquake of March 28. *J Geophys Res* 70(9):2251–2253
- Gao Y, Liu ZZ (2002) Precise ionosphere modeling using regional GPS network data. *J Glob Position Syst* 1(1):18–24
- Hajj GA, Ibañez-Meier R, Kursinski ER, Romans LJ (1994) Imaging the ionosphere with the global positioning system, edited, pp 174–187
- Hansen AJ (1998) Real-time ionospheric tomography using terrestrial GPS sensors. *Proc Inst Nav GPS* 98:717–727
- Hao YQ, Xiao Z, Zhang DH (2013) Teleseismic magnetic effects (TMDs) of 2011 Tohoku earthquake. *J Geophys Res Space Phys* 118(6):3914–3923
- Heki K, Enomoto Y (2013) Preseismic ionospheric electron enhancements revisited. *J Geophys Res Space Phys* 118:6618–6626
- Hernandez-Pajares M, Juan JM, Sanz J (1999) New approaches in global ionospheric determination using ground GPS data. *J Atmos Solar-Terr Phys* 61(16):1237–1247
- Hernández-Pajares M, Juan JM, Sanz J, García-Fernández M (2005) Towards a more realistic ionospheric mapping function. XXVIII URSI General Assembly, Delhi
- Hernández-Pajares M. et al. (2010) Section 9.4 Ionospheric model for radio techniques of chapter 9, Models for atmospheric propagation delays of IERS conventions 2010. In: Petit G, Luzum B (eds) IERS Technical Note No. 36. Verlag des Bundesamts für Kartographie und Geodäsie, Frankfurt am Main
- Howe BM, Runciman K, Secan JA (1998) Tomography of the ionosphere: four-dimensional simulations. *Radio Sci* 33(1):109–128
- Jin SG, Jin R, Li JH (2014) Pattern and evolution of seismo-ionospheric disturbances following the 2011 Tohoku earthquakes from GPS observations. *J Geophys Res Space Phys* 119(9):7914–7927
- Jin SG, Occhipinti G, Jin R (2015) GNSS ionospheric seismology: recent observation evidences and characteristics. *Earth-Sci Rev* 147:54–64
- Kon S, Nishihashi M, Hattori K (2011) Ionospheric anomalies possibly associated with $M \geq 6.0$ earthquakes in the Japan area during 1998–2010: Case studies and statistical study. *J Asian Earth Sci* 41(4–5):410–420
- Kuo CL, Lee LC, Huba JD (2014) An improved coupling model for the lithosphere–atmosphere–ionosphere system. *J Geophys Res Space Phys* 119:3189–3205
- Leonard RS, Barnes RA (1965) Observation of ionospheric disturbances following the Alaska earthquake. *J Geophys Res* 70:1250–1253

- Limberger M, Liang W, Schmidt M, Dettmering D, Hugentobler U (2013) Regional representation of F2 Chapman parameters based on electron density profiles. *Ann Geophys* 31(12):2215–2227
- Liu JY, Chen YI, Chuo YJ, Chen CS (2006) A statistical investigation of pre earthquake ionospheric anomaly. *J Geophys Res* 111(A5):1–5
- Liu JY, Tsai HF, Lin CH, Kamogawa M, Chen YI, Huang BS, Yu SB, Yeh YH (2010) Coseismic ionospheric disturbances triggered by the Chi-Chi earthquake. *J Geophys Res* 115(A8):1–12
- Maruyama T, Tsugawa T, Kato H, Saito A, Otsuka Y, Nishioka M (2011) Ionospheric multiple stratifications and irregularities induced by the 2011 off the Pacific coast of Tohoku earthquake. *Earth Planets Space* 63:869–873
- Nesterov IA, Kunitsyn VE (2011) GNSS radio tomography of the ionosphere: the problem with essentially incomplete data. *Adv Space Res* 47(10):1789–1803
- Oyama KI, Kakinami Y, Liu JY, Kamogawa M, Kodama T (2008) Reduction of electron temperature in lowlatitude ionosphere at 600 km before and after large earthquakes. *J Geophys Res* 113:A11317
- Pryse SE, Kersley L (1992) A preliminary experimental test of ionospheric tomography. *J Atmos Terr Phys* 54(7–8):1007–1012
- Pulinets SA, Boyarchuk KA, Hegai VV, Kim VP, Lomonosov AM (2000) Quasielectrostatic model of atmosphere–thermosphere–ionosphere coupling. *Adv Space Res* 26(8):1209–1218
- Pulinets S, Boyarchuk K (2004) *Ionospheric precursors of earthquakes*. Springer, Berlin
- Rius A, Ruffini G, Cucurull L (1997) Improving the vertical resolution of ionospheric tomography with GPS occultations. *Geophys Res Lett* 24(18):2291–2294
- Saroso S, Liu JY, Hattori K, Chen CH (2008) Ionospheric GPS TEC anomalies and $M \geq 5.9$ earthquakes in Indonesia during 1993–2002. *Terr Atmos Ocean Sci* 19(5):481–488
- Schmidt M, Bilitza D, Shum CK, Zeilhofer C (2008) Regional 4-D modeling of the ionospheric electron density. *Adv Space Res* 42(4):782–790
- Stolle C, Schluter S, Jacobi C, Jakowski N (2003) 3-Dimensional ionospheric electron density reconstruction based on GPS measurements. *Integr Space Geod Syst Satell Dyn* 31(8):1965–1970
- Wen D, Wang Y, Norman R (2012) A new two-step algorithm for ionospheric tomography solution. *GPS Solut* 16(1):89–94
- Yao YB, Chen P, Zhang S, Chen JJ, Yan F, Peng WF (2010) Analysis of pre-earthquake ionospheric anomalies before the global $M = 7.0+$ earthquakes in 2010. *Nat Hazards Earth Syst Sci* 12(3):575–585
- Yao YB, Kong J, Tang J (2015) A new ionosphere tomography algorithm with two-grids virtual observations constraints and 3D velocity profile [J]. *IEEE Trans Geosci Remote Sens* 53(5):2373–2383
- Yavuz E, Arıkan F, Arıkan O (2005) A hybrid reconstruction algorithm for computerized ionospheric tomography. In: *Proceedings of RAST-2005. Recent advances in space research*, HarbiyeAskeriMuze, HavaHarbOkulu, Istanbul, pp 782–787